Energetic electron precipitation characteristics observed from Antarctica during a flux dropout event

Mark A. Clilverd,[1] Neil Cobbett,[1] Craig J. Rodger,[2] James B. Brundell,[2] Michael H. Denton,[3] David P. Hartley,[3] Juan V. Rodriguez,[4,5] Donald Danskin,[6] Tero Raita,[7] and Emma L. Spanswick[8]

Received 24 May 2013; revised 12 September 2013; accepted 14 October 2013; published 5 November 2013.

[1] Data from two autonomous VLF radio receiver systems installed in a remote region of the Antarctic in 2012 is used to take advantage of the juxtaposition of the $L = 4.6$ contour, and the Hawaii-Halley, Antarctica, great circle path as it passes over thick Antarctic ice shelf. The ice sheet conductivity leads to high sensitivity to changing *D* region conditions, and the quasi constant L shell highlights outer radiation belt processes. The ground-based instruments observed several energetic electron precipitation events over a moderately active 24 h period, during which the outer radiation belt electron flux declined at most energies and subsequently recovered. Combining the ground-based data with low and geosynchronous orbiting satellite observations on 27 February 2012, different driving mechanisms were observed for three precipitation events with clear signatures in phase space density and electron anisotropy. Comparison between flux measurements made by Polar-orbiting Operational Environmental Satellites (POES) in low Earth orbit and by the Antarctic instrumentation provides evidence of different cases of weak and strong diffusion into the bounce loss cone, helping to understand the physical mechanisms controlling the precipitation of energetic electrons into the atmosphere. Strong diffusion events occurred as the <600 keV fluxes began to recover as a result of adiabatic transport of electrons. One event appeared to have a factor of about 10 to 100 times more flux than was reported by POES, consistent with weak diffusion into the bounce loss cone. Two events had a factor of about 3 to 10 times more >30 keV flux than was reported by POES, more consistent with strong diffusion conditions.

Citation: Clilverd, M. A., N. Cobbett, C. J. Rodger, J. B. Brundell, M. H. Denton, D. P. Hartley, J. V. Rodriguez, D. Danskin, T. Raita, and E. L. Spanswick (2013), Energetic electron precipitation characteristics observed from Antarctica during a flux dropout event, *J. Geophys. Res. Space Physics*, *118*, 6921–6935, doi:10.1002/2013JA019067.

1. Introduction

[2] The energetic electron fluxes that form the outer radiation belt can be highly dynamic [*Thorne*, 2010; *Horne et al*., 2005] with observed fluxes changing by >3 orders of magnitude on timescales of hours to days [*Morley et al*., 2010]. There are significant uncertainties about the source, loss, and transport of these energetic electrons. Due to their impact on spacecraft systems [*Baker*, 2002] and astronauts [*Maalouf et al*., 2011] as well as polar atmospheric chemistry [*Randall et al*., 2005], the primary research focus has been on energetic electrons with energies >10 keV as well as relativistic electrons (>500 keV). Geostationary satellites, which orbit within the outer radiation belt, can be "upset" or even "killed" by enhanced energetic electron fluxes [*Lam et al*., 2012; *Clilverd et al*., 2012b].

[3] The high dynamism in radiation belt electron fluxes has been associated with geomagnetic storms, although in a complex and nonlinear fashion. Large geomagnetic storms, perhaps correlated with the impact of coronal mass ejection on the magnetosphere, have been observed to cause to very large flux changes, triggering significant acceleration and loss processes [e.g., *Clilverd et al*., 2005; *Horne et al*., 2005]. Weak geomagnetic storms triggered by the arrival of a high-speed solar wind stream interface (SWSI) can also lead to rapid "dropouts" in energetic electron fluxes [*Denton and Borovsky*, 2008; *Miyoshi and Kataoka*, 2008; *Morley et al*., 2010] followed shortly afterward by trapped enhancements

[1]British Antarctic Survey, Cambridge, UK.
[2]Department of Physics, University of Otago, Dunedin, New Zealand.
[3]Department of Physics, University of Lancaster, Lancaster, UK.
[4]Cooperative Institute for Research in Environmental Sciences, University of Colorado Boulder, Boulder, Colorado, USA.
[5]Also at National Geophysical Data Center, National Oceanic and Atmospheric Administration, Boulder, Colorado, USA.
[6]Geomagnetic Laboratory, Natural Resources Canada, Ottawa, Ontario, Canada.
[7]Sodankylä Geophysical Observatory, University of Oulu, Sodankylä, Finland.
[8]University of Calgary, Calgary, Alberta, Canada.

Corresponding author: M. A. Clilverd, British Antarctic Survey (NERC), High Cross, Madingley Rd., Cambridge CB3 0ET, UK. (macl@bas.ac.uk)

©2013. American Geophysical Union. All Rights Reserved.
2169-9380/13/10.1002/2013JA019067

with associated precipitation [*Hendry et al*., 2012] probably reflecting the physics of the acceleration processes which rebuild the fluxes after a dropout. The correlation of high solar wind speed and elevated energetic electron fluxes in the outer radiation belt is one of the most striking aspects of radiation belt dynamics [e.g., *Paulikas and Blake*, 1979].

[4] A major scientific goal is to understand the physical drivers causing radiation belt electron flux dynamics, such that accurate predictive models can be built [*Fok et al*., 2008]. This requires physical understanding of the drivers leading to the enhancements in radiation belt fluxes, as well as the losses, i.e., describing the source and sink terms for the predictive models. Satellites can provide much information on the particle and wave environment. However, geostationary satellites are less well placed to identify the particles losses into the atmosphere because of the difficulty in resolving the pitch angle bounce loss cone (BLC). Geostationary satellites are much better placed to give context to, and describe, the dynamics of the trapped particle populations [*Borovsky and Denton*, 2010; *Hartley et al.*, 2013]. Low Earth orbit (LEO) satellites are usually better able to make observations of electron populations in the BLC but are not geosynchronous and only have short windows of observations in each orbit that are relevant for outer radiation belt research [*Rodger et al*., 2010a]. In this paper we will use data sets from the geosynchronous satellite GOES-13 [*Hanser*, 2011] in combination with the LEO satellites carrying the space environment monitor-2 (SEM-2) detector, i.e., the NOAA POES and the MetOp satellites [*Rodger et al*., 2010a, 2010b]. The electron detectors on POES give a good idea of varying precipitation levels but suffer from uncertainties in their measurement of flux levels due to proton contamination and only partial measurement of the BLC. The electron detectors on GOES are limited to a single point in space, but subsequent calculations of phase space density and the anisotropy of the electron pitch angle distribution can provide further useful clues as to which acceleration and/or loss mechanisms might be operating [*Turner et al*., 2012; *Hartley et al.*, 2013]. Determining, on an event by event basis, how each satellite characterizes the event provides some insight into the physical processes that are occurring.

[5] Outer belt losses occur into the polar atmosphere due to the shape of the geomagnetic field; hence, we have installed a network of radio receivers in the Arctic and Antarctic to monitor these inputs. The Antarctic-Arctic Radiation-belt (Dynamic) Deposition-VLF Atmospheric Research Konsortium (AARDDVARK) receivers use powerful very low frequency (VLF) transmitters [*Gamble et al*., 2008; *Clilverd et al*., 2008b] as radio sources and provide measurements by placing radio receivers at high latitudes in order to sample radio propagation conditions that are influenced by outer radiation belt dynamics [*Clilverd et al*., 2009; *Rodger et al*., 2012]. AARDDVARK is able to significantly enhance the effort of satellite-based research into radiation belt loss mechanisms. This is possible because it uses the fact that VLF radio waves are trapped between the ground and lower ionosphere; energy inputs into the lower ionosphere from the outer radiation belts alter the electrical properties and thus the propagation conditions of received radio waves [*Barr et al*., 2000]. Measuring the perturbation of the radio wave allows a direct calculation of the characteristics of the energetic particle precipitation to be made. The ground-based instruments effectively use the ionosphere as a massive particle detector and thus give a quantitative indication of precipitating electron flux levels but are limited in their ability to place their observations into global context. However, in combination with satellite observations, it is possible to identify the physical mechanisms underlying, and characteristics of, energetic particle losses from the radiation belts. These are the key properties required for the loss terms in predictive models of the radiation belts [*Fok et al*., 2008].

[6] In this study we compare and contrast AARDDVARK ground-based observations of energetic electron precipitation events in Antarctica, which occurred over a moderately active 24 h period, with POES and GOES satellite observations. In the first analysis of data from two Autonomous AARDDVARK systems (solar and wind powered, very remote VLF receivers) installed in the Antarctic in January 2012, we show that bringing together of all of the instruments to study individual events is a powerful technique, yielding significant insight into the radiation belt processes involved. The events studied here occurred during the onset and main phase of a moderate geomagnetic storm in February 2012 where trapped energetic radiation belt electron fluxes are observed to dropout and begin to recover. Different driving mechanisms were observed for the precipitation events with clear signatures in phase space density and electron anisotropy, evidence of periods of weak and strong diffusion into the bounce loss cone, and energy-dependent variations in electron flux enhancements or losses as observed by the satellites.

2. Geomagnetic Conditions

[7] The geomagnetic conditions for the period at the end of February 2012 are shown in Figure 1. In this study we concentrate on three energetic electron precipitation events that occurred on 27 February 2012. In the figure, the solar wind speed and density variations indicate a coronal mass ejection occurred late on 26 February, with the solar wind increasing to ~500 km s^{-1}, and the density increasing by a factor of ~3. A solar wind shock was detected by SOHO at 2107 UT on 26 February, and both *Kp* and *Dst* variations indicate moderately disturbed geomagnetic conditions beginning halfway through 27 February, peaking a few hours before UT midnight with values of $Kp = 5$ and $Dst = -55$ nT. The solar wind speed remained elevated for more than a day before returning to its preevent level.

[8] The conditions described in Figure 1 broadly similar to those studied by *Hendry et al*. [2012] where trapped energetic radiation belt electron fluxes are observed to dropout during small geomagnetic disturbances, triggered by the arrival of an extended period of fast solar wind. *Hendry et al*. [2012] used superposed epoch analysis of low-Earth orbiting POES spacecraft observations to show that dropouts in the trapped flux triggered by a solar wind stream interface (SWSI) are followed ~3 h later by large increases of energetic electron precipitation (EEP) which start as the trapped electron fluxes observed at geostationary orbits begin to recover as acceleration processes become significant. The aim of this paper is to combine ground-based and satellite observations to look in detail at the characteristics of the EEP events that occur around the time of a small radiation belt electron flux dropout.

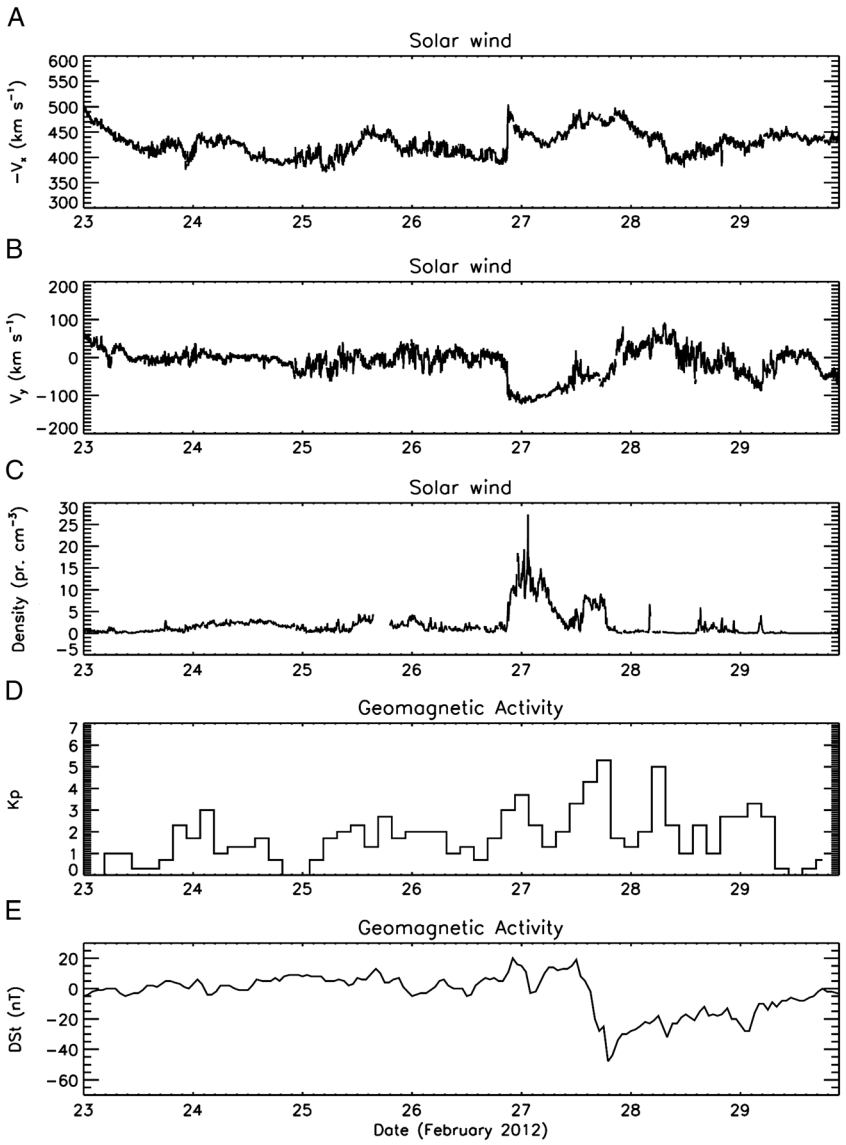

Figure 1. (a–c) The geomagnetic conditions for the period 23–29 February 2012. Solar wind speed and density variations are shown, indicating that a high-speed solar wind event driven by a coronal mass ejection occurred late on 26 February. (d, e) *Kp* and *Dst* variations are shown and indicate moderately disturbed geomagnetic conditions beginning halfway through 27 February, peaking a few hours before UT midnight with values of $Kp = 5$ and $Dst = -55$ nT.

3. Experimental Setup

[9] In January 2012, we deployed low-powered narrow band very low frequency (VLF) radio receivers in two key locations in the Antarctic in order to monitor energetic particle precipitation coming from the outer radiation belt, impacting the great circle path between a transmitter and a receiver. The Autonomous AARDDVARK systems monitor VLF signals from the powerful man-made transmitter located in Hawaii (NPM, 21.4 kHz, 500 kW) to monitor the changes in subionospheric radio wave propagation conditions caused by processes occurring in the outer radiation belt. Combined with an AARDDVARK receiver at Halley [*Clilverd et al*., 2009], Antarctica, the locations selected for the low-powered autonomous receivers make use of a unique geometry that monitors the same radio signal on the same great circle path and at the same geomagnetic latitude at different sites thus providing unprecedented spatial resolution of the lower ionosphere in this region. Figure 2 shows a map of the Antarctic Peninsula region and the locations of the Autonomous AARDDVARK receivers (blue asterisks from left to right, Pine Island Glacier: AA3, Fletcher Ice Dome: AA2) and the Halley receiver (red diamond) with respect to the great circle path of the NPM signal received at Halley (green line). The L shell contours for $L = 4.0$, 4.6, and 7.0 are shown, indicating that the three VLF receivers are located close to the L shell contour at $L = 4.6$ in the region where the path crosses the Antarctic ice shelf at the southern end of the Antarctic Peninsula. For context, we also plot the Southern Hemisphere geomagnetic footprint of the GOES-13 satellite (square), indicating a region rich in measurements despite the extreme remoteness of this part of the Antarctic.

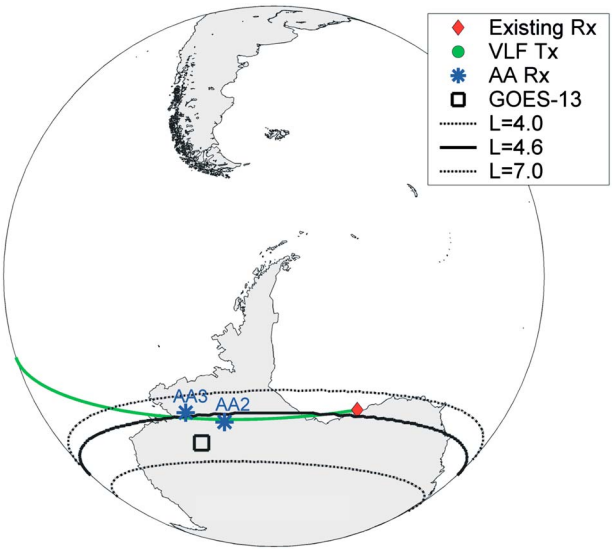

Figure 2. A map of the great circle path (green line) from the Hawaii NPM VLF transmitter to Halley, Antarctica (red diamond). The locations of the two autonomous VLF receivers, labeled AA Rx, are shown (blue asterisks). The Southern Hemisphere geomagnetic footprint of the GOES-13 satellite is also shown (black square), as well as the L shell contours for $L = 4$, 4.6, and 7. The great circle path and the three VLF receivers are located close to the L shell contour at $L = 4.6$ in the region where the path crosses the Antarctic ice shelf at the southern end of the Antarctic Peninsula.

[10] Electron flux data are provided at geostationary orbit ($L = 6.6$) by GOES-13 >800 keV and >2 MeV detectors [*Onsager et al*., 1996]. At the time of this study, GOES-13 was located at 75°W. Thus, the satellite was well positioned to observe the effects of substorm-injected energetic electrons, as well as variations in outer radiation belt electron fluxes, occurring in a similar longitude sector as the ground-based instrumentation. The GOES-13 D3 dome detector provides both the >800 keV and >2 MeV electron fluxes, primarily responding to trapped outer radiation belt particles. The relative variations of the electron fluxes observed at each energy channel are useful for scientific studies. We use the 5 min averaged GOES data which have been corrected for proton contamination and backgrounds.

[11] The magnetospheric electron detector (MAGED) on GOES-13 also provides electron flux measurements in the energy range 30–600 keV. Facing antiearthward, MAGED consists of nine telescopes, a north-south fan as well as an east-west fan. The central telescope of each fan is directed radially antiearthward, while the two fans are oriented at ±35° and ±70° to the central telescope [*Hanser*, 2011]. All telescopes measure flux in five energy channels given as 30–50, 50–100, 100–200, 200–350, and 350–600 keV. The pitch angles of all telescopes are calculated from the relative orientation of the magnetic field measured by the GOES fluxgate magnetometer and the particle velocity defined as the opposite direction to the central look direction of the telescope in question. These pitch angles vary in time. In this study we calculate the pitch angle anisotropy as the ratio between fluxes from 0°–30° (parallel) and between 75°–105° (perpendicular), i.e., $\log_{10}(j_{\text{para}}/j_{\text{perp}})$. Calculation of partial moments for the distribution between 30 and 600 keV also allows estimates of the electron temperature, T (in the parallel and perpendicular directions), and the electron number density, n, to be made:

$$n = 2\pi \iint f_v(\alpha, v) v^2 \sin(\alpha)\, d\alpha\, dv \quad (\text{cm}^{-3})$$

$$T_{\text{para}} = \frac{2\pi m_o}{n} \int f_v(\alpha, v) v^4 \cos^2(\alpha) \sin(\alpha)\, d\alpha\, dv \quad (\text{keV})$$

$$T_{\text{perp}} = \frac{\pi m_o}{n} \int f_v(\alpha, v) v^4 \sin^3(\alpha)\, d\alpha\, dv \quad (\text{keV})$$

where the velocity distribution, f_v, is calculated from the measured differential flux as

$$f_v(\alpha, v) = \frac{m_o}{v^2} j(\alpha, E) \quad (\text{s}^3 \ \text{cm}^{-6})$$

Using the MAGED instrument, we can investigate the behavior of electrons at geostationary orbit in terms of transport away from the satellite and loss from the environment of the satellite (including loss into the atmosphere).

[12] We also make use of particle measurements by the space environment monitor-2 instrument package on board the POES spacecraft which are in Sun synchronous orbits at ~800–850 km altitudes [*Evans and Greer*, 2004]. SEM-2 includes the medium energy proton and electron detector (MEPED), in addition to the total energy detector. Together, these instruments monitor electron fluxes from 50 eV up to 2700 keV. We make use of SEM-2 observations from all 6 POES spacecraft operational at that time. The SEM-2 detectors include integral electron telescopes with energies of >30 keV, >100 keV, and >300 keV, pointed in two directions.

[13] All POES data are available from http://poes.ngdc.noaa.gov/data/ with the full-resolution data having 2 s time resolution. Analysis by *Rodger et al*. [2010a] indicated that the levels of contamination by comparatively low-energy protons can be significant in the MEPED observations. As much as ~42% of the 0° telescope >30 keV electron observations were typically found to be contaminated, although the situation was less marked for the 90° telescope (3.5%). However, NOAA has developed new techniques to remove the proton contamination from the POES SEM-2 electron observations, as described in *Lam et al*. [2010, Appendix A]. This algorithm is available for download through the Virtual Radiation Belt Observatory (ViRBO; http://virbo.org) and has been applied to the SEM-2 observations examined in our study. The 0° pointing detectors are mounted on the three-axis stabilized POES spacecraft so that the center of each detector field of view is outward along the local zenith, parallel to the Earth-center-to-satellite radial vector. Another set of detectors, termed the 90° detectors are mounted approximately perpendicular to the 0° detector. In addition, there is also a set of omnidirectional measurements made from a dome detector which is mounted parallel to the 0° detectors. The detectors pointing in the 0° and 90° directions are ±15° wide, while the omnidirectional dome detectors (termed "omni") are ±60° wide. For the $3 < L < 10$ range, we consider in this study the 90° detector appears to primarily respond to trapped electrons but with pitch angles only a few degrees above the loss cone, and hence, we will refer to it as the "quasi trapped detector," while the 0° detector responds to the electrons in the bounce loss cone and is

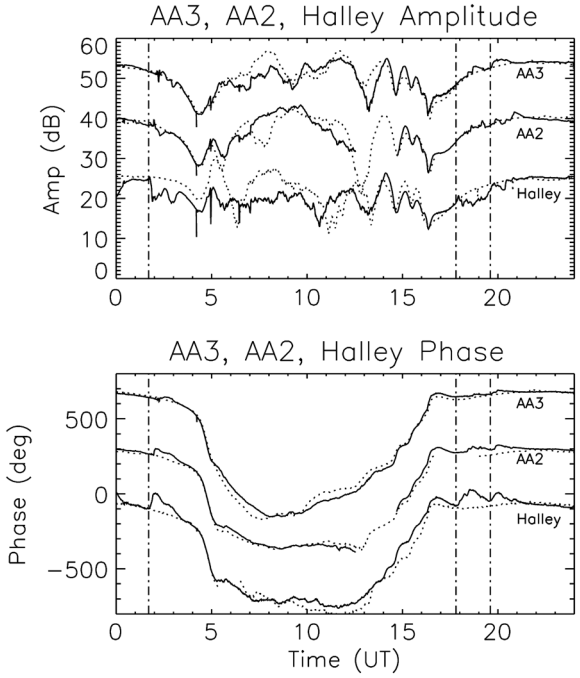

Figure 3. The amplitude and phase variations observed at three sites in the Antarctic (AA3, AA2, and Halley) from the NPM transmitter in Hawaii on 27 February 2012. Typical quiet day curves for each site are shown as dotted lines, and the times of energetic electron precipitation events are identified by vertical dashed lines. The amplitude and phase values have been offset to allow comparison between data sets.

thus referred to as the "BLC detector" (see the modeling in *Rodger et al*. [2010b, Appendix]).

[14] In addition to the electron telescopes, the MEPED instrument also includes a number of proton telescopes. The SEM-2 proton detectors also suffer from contamination, responding to electrons with relativistic energies [*Evans and Greer*, 2004] which can be useful for radiation belt studies [e.g., *Sandanger et al*., 2007; *Millan et al*., 2008; *Rodger et al*., 2010a] outside of solar proton events when significant energetic proton fluxes are present. In particular, the P6 telescope detectors, which are designed to measure >6.9 MeV protons, also respond to electrons with energies in the relativistic range [*Yando et al*., 2011]. In this paper we refer to the P6 telescope as a >800 keV detector, although this is only approximately correct as it implies both high detection efficiencies and a sharp increase in electron detections at an energy of 800 keV. Monte Carlo simulations of the proton telescopes indicate that the P6 telescope exhibits a sensitivity of $G \sim 1.9 \times 10^{-3}$ cm^2 sr at 800 keV and $G \sim 9 \times 10^{-3}$ cm^2 sr^{-1} near 2000 keV [*Yando et al*., 2011]. As shown in Figure 8 of that study, the P6 channel plays a complementary role to the E1–E3 channels for detection of relativistic electrons and is sensitive to electrons of energy larger than roughly 800 keV.

[15] In this study the ground-based Autonomous AARDDVARK data are combined with Halley riometer data. Riometers observe the integrated absorption of cosmic radio noise through the ionosphere [*Little and Leinbach*, 1959], with increased absorption due to additional ionization in the lower *D* region, for example, due to both proton and electron precipitation. The riometer absorption at Halley is provided by a wide beam, 30 MHz, vertically pointing antenna. The dominant altitude of the absorption is typically in the range 70–100 km, i.e., biased toward relatively soft particle energies (~30 keV electrons). Because of their sensitivity to *D* region ionization, the combination of AARDDVARK and riometer data sets are a powerful tool in the analysis of the characteristics of energetic electron precipitation events [*Rodger et al*., 2012]. In order to provide wider geographical context for the precipitation events studied in this paper, we make use of riometer data from Fort McMurray, Canada (56.7°N, 111.2°W, $L = 5.5$), and Sodankylä, Finland (67.4°N, 26.4°E, $L = 5.1$). Both these riometer systems have a wide beam, 30 MHz, vertically pointing antenna.

4. Results

[16] On 27 February 2012, at least three energetic electron precipitation events occurred and their impacts on the ionosphere were captured by the Autonomous AARDDVARK systems in the Antarctic. Figure 3 shows the amplitude and phase of the NPM transmitter received at (in order of increasing distance from Hawaii) AA3, AA2, and Halley. The top shows the diurnal amplitude variation on 27 February as a solid line, with a representative quiet day curve shown as a dotted line. The amplitude levels from each receiver site have been offset in order to allow some differentiation between the sites. Three vertical dashed lines indicate the start of the three events under study, which can be seen as departures from the quiet day curve lasting about 1–2 h (which we will call the 02, 18, and 20 UT events after their approximate start times). The bottom is of a similar format but with the diurnal phase variations shown. Again, a phase offset has been applied in order to allow some differentiation between the sites.

[17] From looking at the overall amplitude and phase variations around the times of the three events indicated (~02, 18, and 20 UT), we can tell that the propagation conditions prior to the events were essentially ones of daytime along the whole great circle path. This can be determined by the amplitude variations at all three sites between 16 and 04 UT, and the characteristic daytime phase advances at 14–17 UT associated with sunrise conditions on the great circle path. Because of the event timing, we are able to model the preevent propagation conditions using the long wave propagation code (LWPC) [*Ferguson and Snyder*, 1990], after applying the appropriate daytime *D* region electron density profile parameterization as set out in *McRae and Thomson* [2000] and *Thomson et al*. [2011a, 2011b]. The profile parameterization varies along the great circle path as a function of solar zenith angle. The VLF analysis/modeling is less uncertain during the daytime because the propagation conditions are more reproducible than during nighttime conditions.

[18] The deployment of the Autonomous AARDDVARK systems was planned to take advantage of the juxtaposition of the $L = 4.6$ contour and the NPM-Halley great circle path as shown in Figure 2. From AA3 to Halley, the propagation path is quasi constant in L shell ($L \sim 4.6$) and passes over thick Antarctic ice shelf. The low ice sheet conductivity will result in a high sensitivity to changing *D* region conditions [*Westerlund et al*., 1969], and the quasi constant L shell will focus on electron precipitation that is driven by outer radiation belt processes. Prior to reaching AA3, the propagation

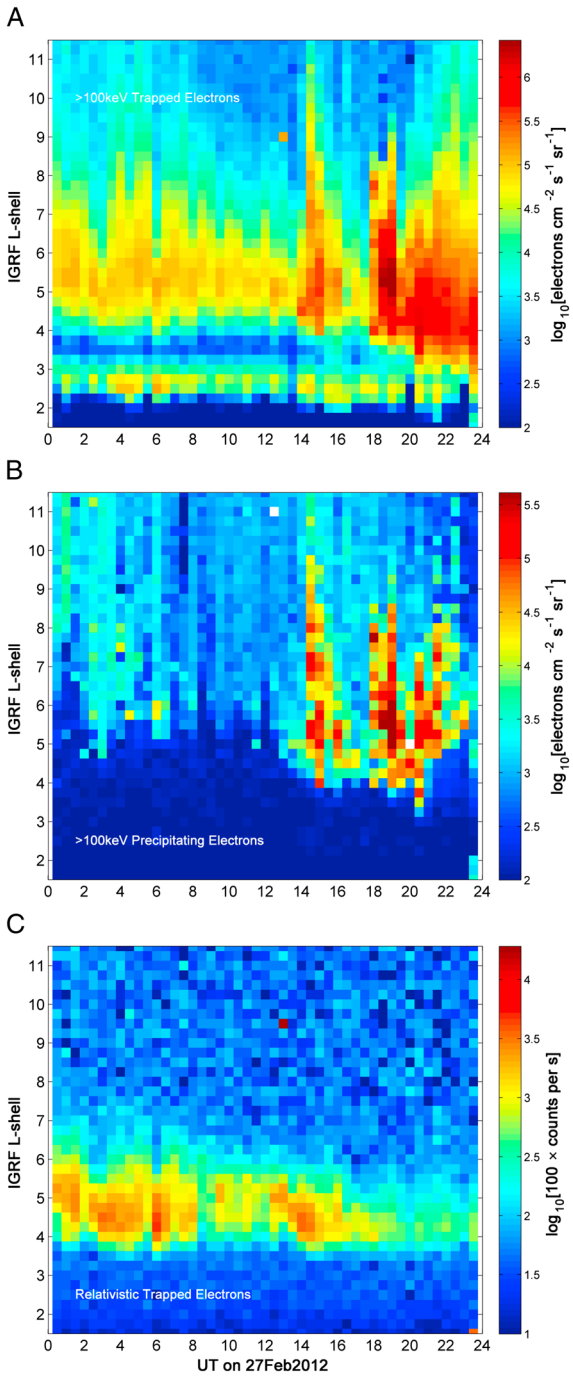

Figure 4. POES electron flux observations for 27 February 2012. (a) POES >100 keV trapped fluxes. (b) POES >100 keV BLC fluxes. (c) POES relativistic trapped electron fluxes (energies larger than about 800 keV).

path from NPM, Hawaii, crosses the sea and experiences few effects of precipitating electrons from the outer radiation belt because the majority of the path is at very low L shell [*Clilverd et al.*, 2005]. This part of the great circle propagation path is much less sensitive to energetic electron precipitation. In this respect, we would anticipate that most of the observed perturbations are generated on the great circle path between AA3 and Halley, and this is borne out by the observation of only small effects observed at AA3, while larger effects are observed at Halley during the event periods shown in Figure 3.

[19] In order to put the three precipitation events into some sort of context, we show zonally averaged POES data for 27 February 2012 in Figure 4. Figure 4a shows the variations observed at LEO in the quasi trapped fluxes of >100 keV electrons from $L = 2$–8. The enhanced fluxes associated with the outer radiation belts occur at $L \approx 4$–8, while the slot region can be seen at $L \approx 3$–4. During two of the events (18 UT and 20 UT), enhanced quasi trapped fluxes are observed with fluxes increasing from $\sim 10^4$ el cm^{-2} s^{-1} sr^{-1} to $\sim 10^6$ el cm^{-2} s^{-1} sr^{-1}, and the L shell range of enhanced fluxes increasing to $L \approx 3.5$ to $L > 8$. The earliest event (02 UT) does not show any increase in quasi trapped fluxes, rather a relatively indistinct decrease in flux levels at higher L shells ($L \approx 6$–8). Overall, this figure suggests that the trapped >100 keV electron flux decreases during the second half of the day, with noticeably reducing background outer radiation belt fluxes. The 02 UT event seems to have little long-term effect on the trapped fluxes, while the 18 and 20 UT events coincide with a significant long-term increase in the trapped fluxes. As there is a weak solar proton event ongoing during 27 February 2012, we checked the POES P5 data (2.5–6.9 MeV protons) to see if the enhancements seen in the >100 keV electrons could be due to proton contamination. POES P5 indicates smoothly reducing fluxes of protons for $L > 5$ from 00 UT to 24 UT on 27 February, with no suggestion of enhancements at 18 or 20 UT and thus no sign of any significant proton contamination in the electron data shown. The $L > 5$ distribution of the low 2.5–6.9 MeV proton fluxes on 27 February 2012 is consistent with the influence of rigidity cutoff effects and suggests that the >800 keV electron fluxes at $L < 5$ shown in Figure 4c are not generated by protons.

[20] Figure 4b shows the variation of the >100 keV electron BLC fluxes. Enhanced electron precipitation fluxes are observed at 02, 18, and 20 UT, coincident with the radio wave data, but the 02 UT event is much weaker in the POES data than the 18 and 20 UT events where precipitating flux levels are an order of magnitude larger and extend over a wider range of L shells. The 02 UT event is only noticeable because of the fact that the precipitation signature is stronger at $L \approx 4$–5.5 than the immediate background levels.

[21] Figure 4c shows the variation of the trapped relativistic electron fluxes (>800 keV) from the P6 telescope. The relativistic electron fluxes show a decrease of about a factor of 10 in the outer radiation belt starting at ~13 UT, initially at higher L shells, this is concurrent with the onset of the main phase of the moderate disturbance described in Figure 1, and similar to the decreases seen in the >100 keV trapped fluxes. The decline of the outer radiation belt fluxes over the period 13–16 UT is consistent with the superposed epoch analysis reported by *Hendry et al.* [2012], suggesting that this behavior can be considered to be a small radiation belt dropout event. However, no recovery is seen in the relativistic fluxes after the 18 and 20 UT events, unlike that seen in the >100 keV trapped fluxes. There is also a suggestion that the relativistic fluxes decrease during the 02 UT event, particularly at $L \approx 6$.

[22] In this study there are two L shell ranges to consider. One is at geosynchronous orbit ($L \sim 6.6$) where GOES-13 can provide insight into the conditions in the radiation belt,

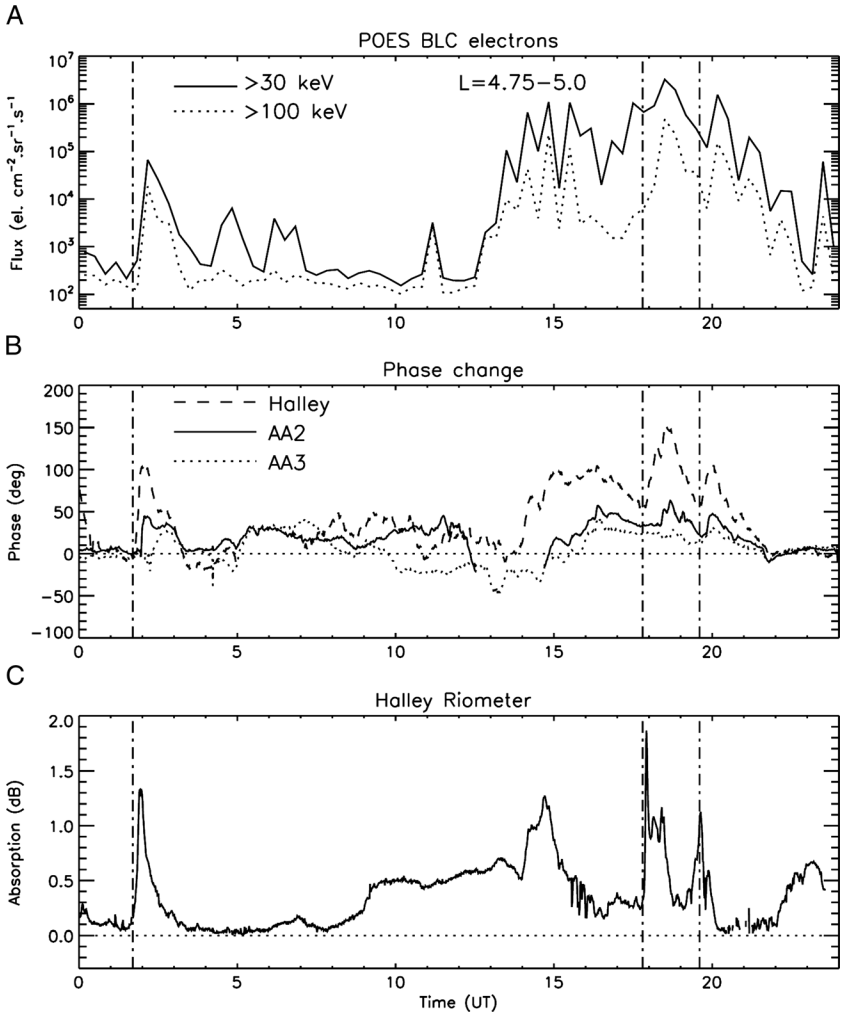

Figure 5. (a) POES BLC electron fluxes (>30 keV and >100 keV) over the range $L = 4.75$–5.0 on 27 February 2012. (b) AARDDVARK phase perturbations at Halley (dashed lines), AA2 (solid lines), and AA3 (dotted lines). (c) Halley riometer absorption. The times of the three study events are indicated by the vertical dashed lines.

and the other is the latitude range from $L = 4.5$–5.0 which covers the L shells of the ground-based instrumentation. Figure 5 shows the diurnal variation of the NPM phase perturbation observed at AA3 (dotted line), AA2 (solid line), and Halley (dashed line) in Figure 5b, and the Halley riometer absorption in Figure 5c. The times of the three events (02, 18, and 20 UT) are indicated by vertical dashed lines. In both data sets, the perturbations are shown relative to a typical quiet day curve for the time of year. Figure 5a shows the POES >30 keV (solid line) and >100 keV (dotted line) electron fluxes observed in the BLC over the range $L = 4.75$–5.0. The three panels show good consistency in that elevated electron precipitation fluxes are observed by both energy channels in POES at the same times as increased *D* region ionization is detected by the AARDDVARK and riometer experiments.

[23] In the riometer panel, there are four distinct peaks in absorption at Halley, all of which have levels that are ~1 dB. Three are identified as events studied in this paper and have relatively sudden onsets (the 02, 18, and 20 UT events). The fourth absorption peak exhibits a more gradual onset before reaching a maximum at ~14–15 UT. Similar features can be seen in the NPM phase data (Figure 5b) and the POES fluxes (Figure 5a). In this study we concentrate on the events which are clearly identified by their sudden onsets as this allows us to identify the events more readily in the different data sets. In Figure 5a, it is clear that the precipitation fluxes involved in the 02 UT event are smaller by a factor of ~40 than the fluxes involved in the 18 and 20 UT events (8×10^4 at 2 UT cf. 3×10^6 el cm^{-2} s^{-1} sr^{-1} at 18 UT). This is inconsistent, not only with the Halley riometer peak absorption levels, but with the Halley phase perturbations which are close to 100° in all four cases, suggesting similar precipitating fluxes into the atmosphere in all of the cases. The phase perturbations at AA2 are also typically the same value for all of the events, i.e., ~50°, while AA3 shows similar consistency at ~25°. Understanding this difference, between the ground-based observations and satellite measurements, is a key to using these instruments to understand the physical mechanisms controlling the precipitation of energetic electrons into the atmosphere.

[24] In both Figures 4a and 4b, the >100 keV trapped electron and BLC flux data show an enhancement at ~14–15 UT. In Figure 5, there are also increases in >30 keV fluxes,

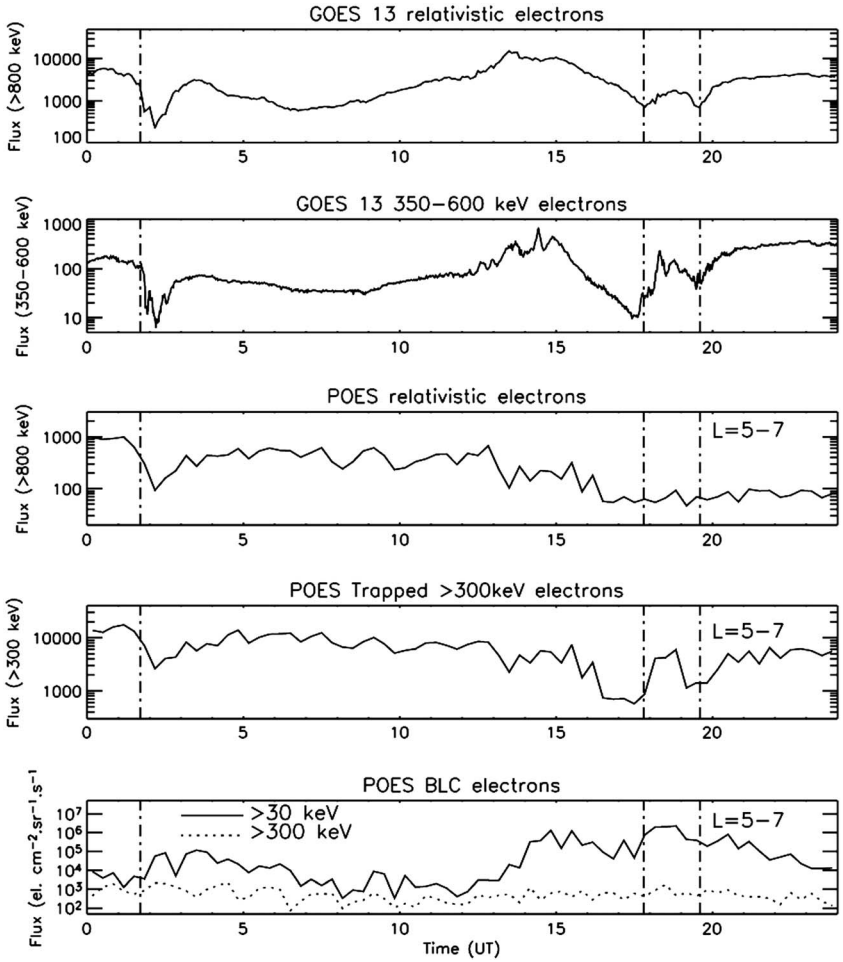

Figure 6. (top to bottom) The GOES-13 >800 keV electron fluxes, GOES-13 350–600 keV electron fluxes, POES >800 keV trapped electron flux over the $L = 5$–7 range, POES trapped >300 keV electron flux in the range $L = 5$–7, the POES >30 keV, and >300 keV BLC electron fluxes over the range $L = 5$–7. Times of the electron precipitation events under study on 27 February 2012 are indicated by vertical dashed lines. Some similarities between the GOES-13 and POES trapped fluxes can be seen. See text for more details.

AARDDVARK phase, and riometer absorption at ~14–15 UT. Although this event appears to be the first significant enhancement of trapped fluxes in the outer radiation belt following the onset of the geomagnetic storm, we do not analyze it in detail, as it occurs during the complex sunrise period in the Autonomous AARDDVARK data and is very difficult to model as a result. However, the characteristics of the ~14–15 UT event are similar to those of the 18 and 20 UT events, in that there appears to be a phase perturbation of ~100° at Halley, POES BLC fluxes >30 keV of ~10^6 el cm^{-2} s^{-1} sr^{-1}, and a riometer absorption level of ~1 dB. Unlike the 18 and 20 UT events, Figure 4 shows that the >100 keV trapped fluxes do not remain enhanced but return toward preevent levels, and therefore, the processes that generated the enhancement in trapped and BLC fluxes do not appear to have any long lasting influence on the outer radiation belt.

[25] In Figure 6, we compare the geosynchronous GOES-13 data and zonally averaged POES electron data over the equivalent range, $L = 5$–7, during 27 February 2012. As we stated before, the GOES-13 data are representative of trapped fluxes, while POES can provide information on precipitating (BLC) and quasi trapped electron fluxes. The times of the three events are identified by vertical dashed lines.

[26] The response of the trapped electron fluxes during the 02 UT event in this data set is one of a decrease by a factor of ~10. This is observed by GOES-13 in the 350–600 keV channel, as well as the >800 keV channel. POES sees similar behavior in the >300 keV and the >800 keV channels. Electron precipitation measured by POES is enhanced during the 02 UT event, particularly at energies of >30 keV, but at >300 keV, there is little variation to be seen, with fluxes close to the instrument noise floor most of the day. Overall, the picture at 02 UT is one of loss of trapped fluxes from the outer radiation belt over a wide range of energies, with enhanced electron precipitation into the atmosphere as a loss mechanism, particularly for the lower energy electrons. At higher energies, it is not possible to use POES P6 to determine if electron precipitation is occurring or not because it is close to its sensitivity level.

[27] The responses of the trapped electron fluxes during the 18 and 20 UT events are quite different to the 02 UT event. GOES-13 and POES trapped fluxes show increases in the 350–600 keV and >300 keV channels, respectively. While

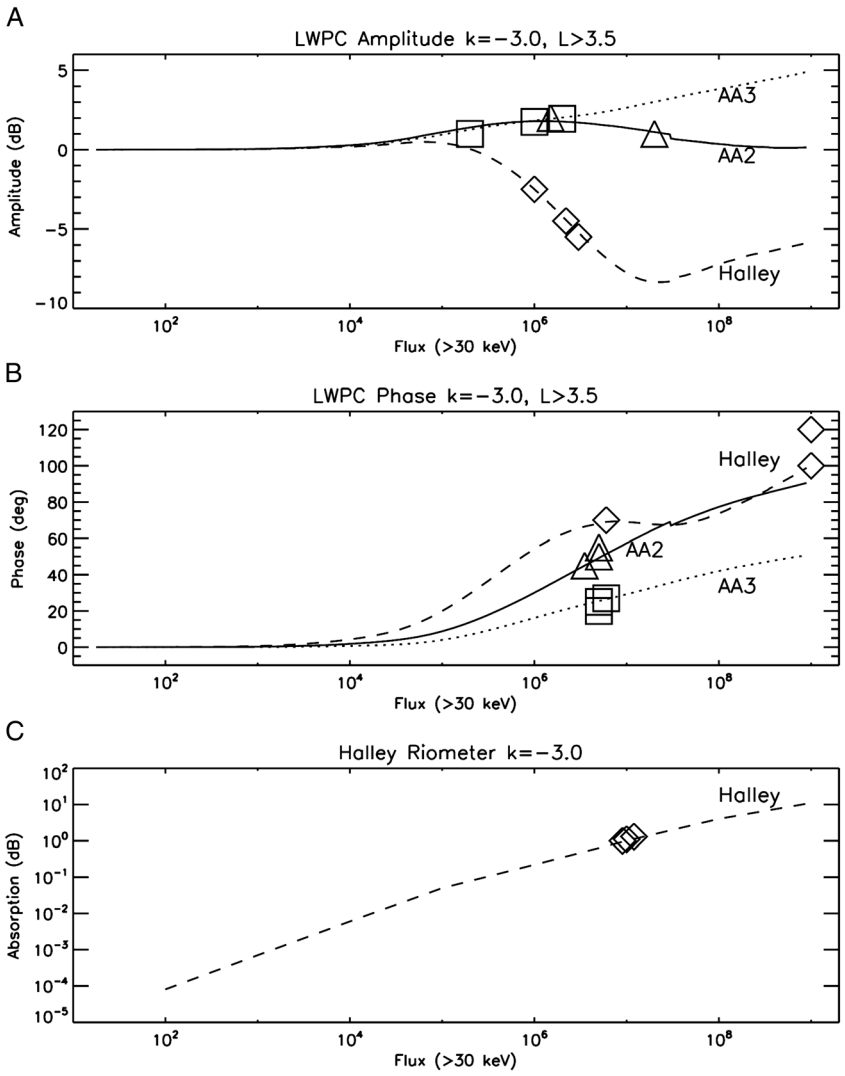

Figure 7. (a) The NPM amplitude perturbation as a function of electron integral precipitation flux >30 keV, for a $k=-3$ power law spectra. The precipitation covers the great circle path from $L=3.5$ to AA3 (dotted line), to AA2 (solid line), and to Halley (dashed line). Square symbols represent the three-event perturbation levels as measured at AA3, triangles represent perturbation levels at AA2, and diamonds at Halley. (b) The same format as in Figure 7a but for the NPM phase perturbation. (c) The same format as Figures 7a and 7b but for the Halley riometer absorption level. See text for more details.

the GOES-13 >800 keV channel also shows small increases after the onset of the two events, this does not happen for the equivalent POES energy range. However, the POES relativistic electron detector has nearly an order of magnitude more sensitivity at 1.5 MeV than at 0.5 MeV [*Yando et al*., 2011], suggesting that the extended flux dropout is probably occurring for energies of >1 MeV rather than <1 MeV.

[28] The $L=5$–7 precipitating electron fluxes at >30 keV are elevated during the 18 and 20 UT events, although as with the 02 UT event, the >300 keV fluxes are unchanged and at the instrument noise floor. Clearly, these events differ from the 02 UT event in that the later two events appear to be cases where the electron precipitation is occurring at the same time as the increase in trapped fluxes, and therefore, the precipitation appears to be a consequence of the enhanced fluxes, which could have occurred either through acceleration processes which also causes losses or losses from the transport and energization of electrons within the radiation belts. We discuss the evidence for these two different ideas in the following section.

5. Discussion

5.1. Ground-Based Observations

[29] *Clilverd et al*. [2008a, 2012a, 2012b] combined riometer absorption data and AARDDVARK radio wave data to estimate the electron precipitation flux occurring during substorms. A more detailed description of this technique can be found in *Clilverd et al*. [2008a], so we provide only an outline of the process here. We undertake the calculation of electron precipitation flux using the NPM daytime phase and amplitude perturbations from AA3, AA2, and Halley, and the Halley riometer observations. By comparing the observed fluxes for the 02, 18, and 20 UT events with the flux responses calculated for the NPM amplitudes, NPM phases,

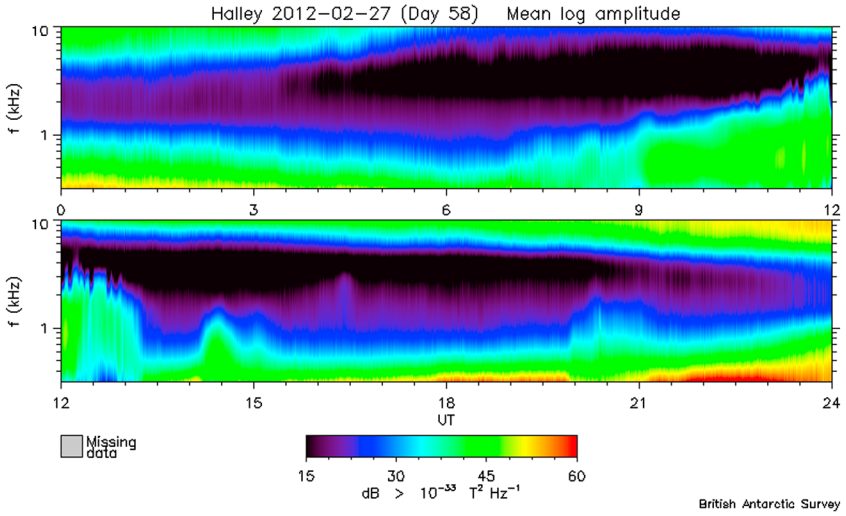

Figure 8. Halley 0.5–10 kHz wave intensity on 27 February 2012. Of the three electron precipitation events studied (02, 18, and 20 UT), only the 20 UT event is associated with the occurrence of enhanced 1–2 kHz waves.

and riometer absorption, we can identify the actual precipitating flux for each event.

[30] Energetic electron precipitation produces mesospheric ionization, and its resulting effects on VLF wave propagation can be modeled using the long wave propagation code (LWPC). LWPC models VLF signal propagation from any point on Earth to any other point. Given electron density profile parameters for the upper boundary conditions, LWPC calculates the expected amplitude and phase of the VLF signal at the reception point. A more detailed description of this technique can be found in *Clilverd et al*. [2008a]. In *Clilverd et al*. [2010], a fit was made to DEMETER electron spectra from ~90–700 keV in terms of a power law where the slope (scaling exponent, k) typically ranged from -1 to -3. A power law slope of $k=-3$ represents the LANL-97A substorm spectra in *Clilverd et al*. [2008a] and the Galaxy 15 substorm spectra in *Clilverd et al*. [2012b]. The ionospheric electron density profile is found by introducing an additional ionization source from the electron precipitation in a simple ionospheric model to describe the balance of electron number density, N_e, in the lower ionosphere. This simple electron density model is based on that given by *Rodger et al*. [1998], which was further developed by *Rodger et al*. [2007, 2012].

[31] In addition, we can calculate the Halley riometer absorption from the same electron number density as was applied to LWPC. By calculating height-integrated differential absorption using the method described in *Rodger et al*. [2012], we can estimate the Halley riometer absorption generated by the same energetic electron precipitation characteristics used in the VLF modeling runs.

[32] Figure 7 shows the results of the calculations using a wide range of >30 keV electron flux magnitudes. Figure 7a shows the calculated NPM amplitude perturbation at AA3 (dotted line), AA2 (solid line) and Halley (dashed line) for a power law spectrum with the gradient $k=-3$ suggested by previous authors (see text above). The gradient was also consistent with that determined from a fit to the three POES electron channels (>30, >100, and >300 keV). The flux was varied from 10^1–10^9 >30 keV el cm^{-2} s^{-1} sr^{-1}. The peak perturbation values for each of the 02, 18, and 20 UT events plotted on the panel with AA3 (squares), AA2 (triangles), and Halley (diamonds) are represented by separate symbols. Figure 7b is the same format as Figure 7a but represents the NPM phase changes. Figure 7c is also a similar format but only shows the riometer absorption calculations for Halley and not AA3 and AA2. In all three panels of this figure, the symbols representing the observations were placed in order to fit the observations to the modeling calculations. For some observations (like the amplitude changes observed at AA3), the dependence of the amplitude change is very weak, which would lead to a large error in flux even if the measurement error was small. From this figure, we can see that the calculated VLF response to increasing flux levels (with a constant spectrum) is different at each site, with amplitudes increasing at AA3 and AA2, but decreasing at Halley. However, at all three sites, the NPM phase perturbation increases as the precipitation flux increases. Similarly, the riometer absorption increases smoothly with increasing precipitation flux. For all three parameters shown, significant responses are only seen once the >30 keV precipitating fluxes exceed 10^5 el cm^{-2} s^{-1} sr^{-1}.

[33] The scatter of observations during the events ranges from flux levels of 10^5–10^9 for >30 keV electron precipitation, with the majority suggesting fluxes of 10^6–10^7 el cm^{-2} s^{-1} sr^{-1}. No clear distinction can be made between the flux estimates of any of the three events, as the ground-based data suggest that these three events are of similar magnitude, as noted earlier. There are two significant outliers in this analysis, namely the ~100° and 120° phase changes observed at Halley during the 02 and 18 UT events. These values give very large fluxes which are at odds with the other data during the same events. At the time of writing, it is apparent that the phase change values have been accurately measured, but it is unclear why they are so large in comparison with the modeling results expected for fluxes of 10^6–10^7 el cm^{-2} s^{-1} sr^{-1}.

[34] These results confirm the earlier observation that suggested that the POES BLC flux observations during the

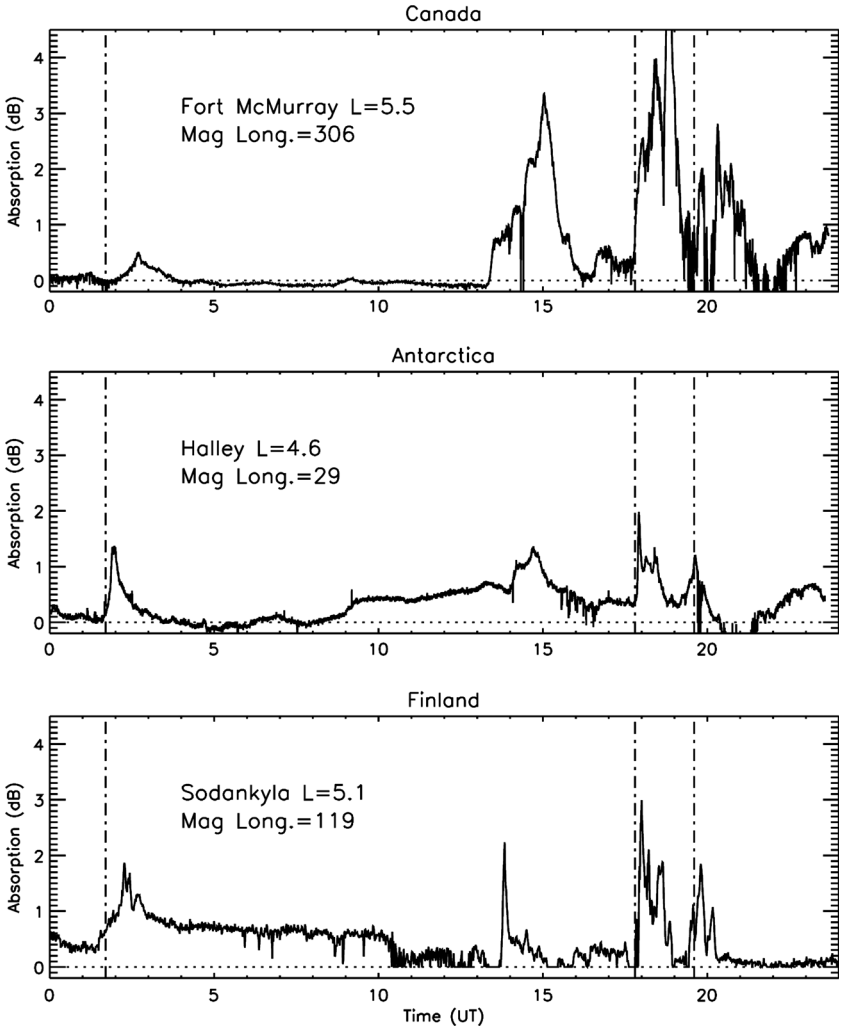

Figure 9. Riometer absorption levels during 27 February 2012, spanning ~180° of magnetic longitude at $L \sim 5$. The stations in Canada, Antarctica, and Finland show similarities in the occurrence of periods of excess ionization at the 3 times of interest (indicated by the vertical dashed lines), although there are notable differences in absorption level and structure at times.

02 UT event were surprisingly low. The modeling calculations for the AARDDVARK and riometer instruments suggest that if the POES >30 keV BLC fluxes of 8×10^4 el cm^{-2} s^{-1} sr^{-1} were correct, then neither ground-based instrument would have registered an observable perturbation starting at 02 UT. Clearly, this was not the case. For the 18 and 20 UT events, the POES >30 keV BLC fluxes (3×10^6 el cm^{-2} s^{-1} sr^{-1}) are similar to the modeling calculations, and thus, POES observations represent a reasonable description of the electron precipitation during those events. *Rodger et al*. [2010a] described in detail some of the issues surrounding the difficulties in using POES BLC measurements. One significant aspect that we note here is that the detector is not usually measuring the whole of the BLC, but only a fraction of it. This is particularly true for observations made at $L > 2$. Thus, in the case of the 02 UT event, we can assume that the POES BLC measurement is not representative of the whole electron population within the BLC and is, in fact, missing a large proportion of it. This is consistent with the effects of a weak diffusion process [*Horne*, 2002] which only pushes electrons into the BLC close to the outer edge of the loss cone (in pitch angle space) and not all the way into the detector viewing angle (i.e., the pitch angle range sampled by the BLC detector). This mechanism was also suggested to explain the observations during a VLF chorus event described in *Clilverd et al*. [2012b]; however, in the 02 UT event, no chorus waves were observed by the Halley VLF/ELF Logger Experiment (VELOX) instrument [*Smith*, 1995]. We also note here that the 02 UT event was not associated with any Pc 1–2 waves at Halley using the Augsburg College search coil magnetometer [*Engebretson et al*., 2008] and that neither of the 18 or 20 UT events show coherent Pc 1–2 wave power. In Figure 8, we show the 0.5–10 kHz wave intensity received by the VELOX instrument at Halley on 27 February 2012. Waves in the ranges 6–10 kHz and 0.5–0.6 kHz are typically associated with distant lightning impulses, while waves in the range 0.6–6 kHz are likely to be chorus or plasmaspheric hiss. Of the three events studied here, only the period associated with the 20 UT event shows an enhancement in 1–2 kHz chorus wave power at Halley. However, there is also an enhancement in 1–2 kHz wave intensity at ~14 UT, coincident with the ~14–15 UT precipitation event discussed previously.

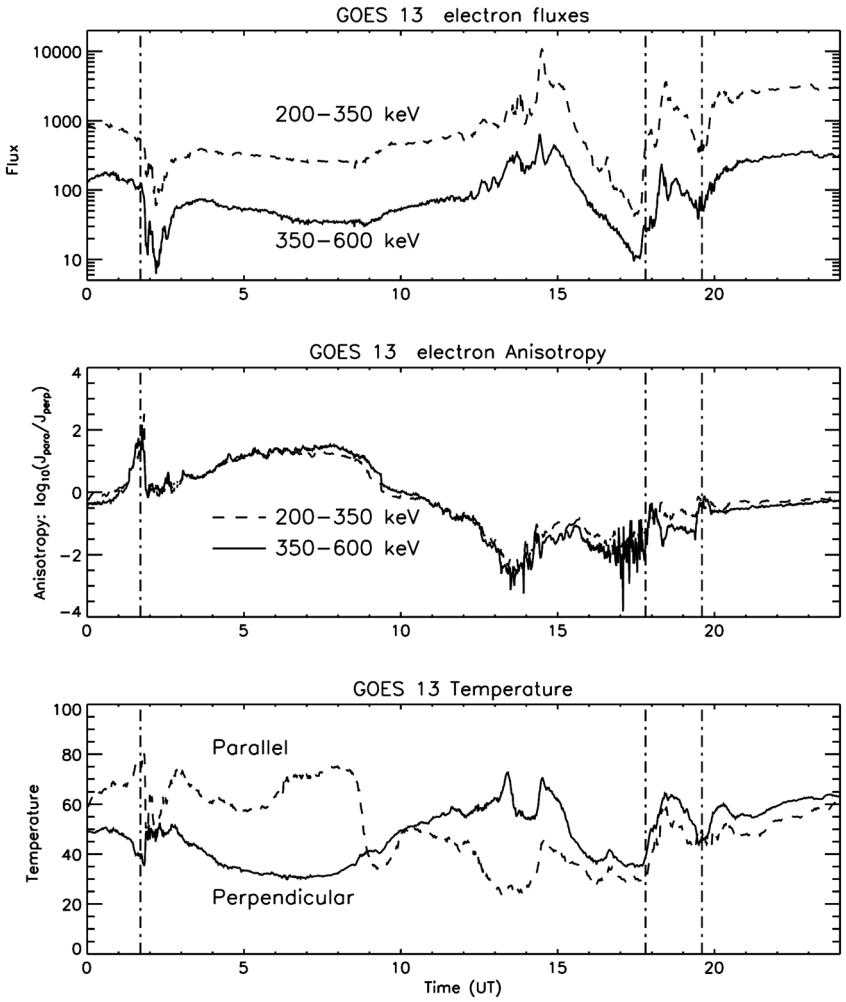

Figure 10. (a) The GOES-13 200–350 and 350–600 keV electron flux channels (cm^{-2} s^{-1} sr^{-1} keV^{-1}) during 27 February 2012. At the times of the perturbations under study (shown by vertical dashed lines) decreases and increases in flux are observed in both energy channels. (b) The electron anisotropy in the two energy channels. The electron precipitation event at ~02 UT shows a marked change in anisotropy, whereas the two later events show less systematic variations. (c) The GOES-13 parallel and perpendicular temperature (keV) over the same period.

[35] Another possibility that could explain the disparity between POES and the ground-based instruments during the 02 UT event is that the region of precipitation is localized to the longitudes of Halley, and thus, the zonally averaged POES data are underestimating the actual flux involved. In order to investigate this, we undertook two checks. The first was to look at the location of the POES satellites when they detected an enhancement in BLC flux at ~02 UT, and the second was to determine if riometers at different longitudes around the world also saw the 02 UT event. In the first check, we found that POES detected enhanced BLC flux at ~02 UT with a uniform scatter around the globe and that the majority of observations consisted of peak values of 1×10^4 to 4×10^4 el cm^{-2} s^{-1} sr^{-1}. None gave flux values of 10^6, although the highest flux was reported as 6×10^5 el cm^{-2} s^{-1} sr^{-1} at a southern longitude about 70° east of Halley.

[36] For the second check, Figure 9 shows the riometer data from three geomagnetic longitudes for 27 February 2012. The three event times are indicated by vertical dashed lines, and details of the site name, L shell, and geomagnetic longitude are given in each panel. The sites Fort McMurray, Halley, and Sodankylä all show some indication of the three electron precipitation events, although with different absorption levels. Typically, Halley shows the smallest absorption levels for the events. Sodankylä to the east of Halley shows the largest absorption during the 02 UT event, consistent with the POES longitudinal picture, but also with absorption levels suggestive of precipitation fluxes significantly higher than POES. Thus, the riometer signature at Halley does not provide an overestimate of the actual flux involved, and POES is genuinely underreporting the precipitation fluxes.

[37] Overall, the ground-based data suggest that the three events studied have precipitation fluxes of 10^6–10^7 el cm^{-2} s^{-1} sr^{-1} for >30 keV electrons. The 02 UT event appears to have a factor of ~10–100 times more flux than was reported by POES, consistent with weak diffusion into the BLC. The 18 UT and 20 UT events only have a factor of <10 times more >30 keV flux than was reported by POES, much more consistent with strong diffusion conditions.

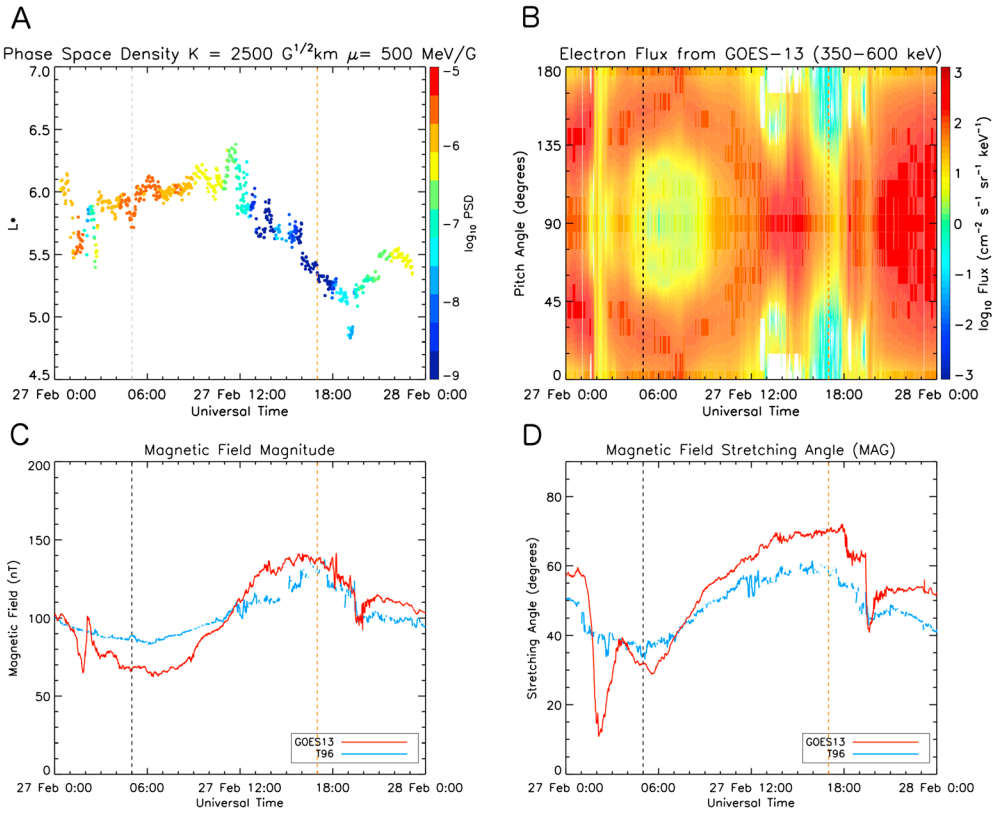

Figure 11. (a) Phase space density as a function of the three adiabatic invariants during 27 February 2012, calculated using GOES-13 observations and T96 [*Tsyganenko and Stern*, 1996] magnetic field model. (b) Pitch angle distribution from GOES-13 for 350–600 keV electrons during 27 February 2012. (c) A comparison of the measured magnetic field magnitude and that produced by the T96 model. (d) A comparison of the measured magnetic field stretching angle, defined as $\vartheta_{\text{stretch}} = \arctan\left(B_Z/\left(B_X^2 + B_Y^2\right)^{1/2}\right)$, and that produced by the T96 model in geomagnetic coordinates. In all panels, the vertical dashed lines indicate local magnetic midnight (5 UT) and noon (17 UT) for GOES-13.

5.2. GOES-13 Observations

[38] It has been shown that the three EEP events are observed over a range of L shells including those of the geostationary satellite GOES-13. As such, the detailed observations from the GOES-13 MAGED instrument, in addition to magnetometer data, can be used to investigate in detail what mechanisms or process might be taking place. Figure 10 shows the electron flux, and anisotropy (defined as $\log_{10}(j_{\text{para}}/j_{\text{perp}})$) for two energy channels, 200–350 keV and 350–600 keV, during 27 February 2012. In general, the anisotropy would be expected to be more parallel (positive) on the nightside and more perpendicular on the dayside (negative) due to drift shell splitting. Superposed on this behavior may be more short-term changes caused by processes such as those leading to the three EEP events under study here. The bottom panel shows the parallel and perpendicular temperature derived for the whole energy range (50–600 keV). The times of the three events are indicated by three vertical dashed lines.

[39] For the 02 UT event (nightside: ~21 LT), both energy channels show a decrease in flux about an hour in duration. At the event onset, the anisotropy, which had been steadily increasing over the preceding hour, indicating an increasingly parallel oriented distribution, suddenly drops back toward zero, indicating an isotropic distribution. At onset, the parallel electron temperature decreases, while the perpendicular electron temperature increases slightly. These observations suggest a loss of electrons over a wide energy range, with the reduction of parallel temperature and sudden decrease of anisotropy supporting the idea of the precipitation of parallel-orientated electrons into the atmosphere.

[40] However, for the 18 and 20 UT EEP events (dayside: 13 and 15 LT), the observations in Figure 9 indicate quite different behavior when compared with the 02 UT event. The electron fluxes over the 200–600 keV energy range exhibit an increase rather than a decrease at the event onset, while the anisotropy returns to near zero (approximately isotropic distribution) from small negative values (slightly perpendicularly oriented distribution) rather than large positive ones (parallel-oriented distribution). The parallel and perpendicular electron temperatures both increase. These observations suggest an overall increase in flux over a wide energy range, which includes parallel-propagating electrons. Rather than a loss mechanism, the 18 and 20 UT EEP events appear to be part of a transport process as indicated by the L* variation in Figure 11 (top).

[41] We investigate these ideas further by calculating the phase space density (PSD) using techniques described by *Selesnick and Blake* [2000] and *Green and Kivelson*

[2004], accounting for the physical behavior of the electrons as a function of the three adiabatic invariants (μ, K and L*). Figure 11 shows the PSD plotted as a function of L* and time during 27 February 2012, for constant μ and K (chosen μ value corresponds to the 350–600 keV electron channel from GOES-13, chosen K value corresponds to more parallel-oriented electrons), in addition to the full pitch angle distribution for 350–600 keV electrons from GOES-13 and a comparison of the magnetic field measured by GOES-13 and the output of the T96 magnetic field model [*Tsyganenko and Stern*, 1996] used in the PSD calculation. The vertical dashed lines indicate the times of magnetic midnight and noon at the satellite. During the 02 UT EEP event, the calculated phase space density reduces by ~2 orders of magnitude from an initial high level while there is little variation in L*. The magnetometer data indicate large stretching of the magnetic field, with a subsequent dipolarization occurring around 02 UT (suggestive of substorm activity). Electron flux rapidly decreases and then recovers across all pitch angles. The PSD reduction at this time indicates that any electron losses are unlikely to be driven by adiabatic transport and may be due to loss to the atmosphere (although it is noted that PSD calculations are limited by the accuracy of the implemented magnetic field model).

[42] The 18 and 20 UT EEP events occur as the spacecraft moves from noon toward dusk and in a regime of low PSD with large L* variation, indicating the likelihood of adiabatic transport of electrons is occurring. Onset times for these events are approximately coincident to step changes in the magnetic field stretching angle. The 20 UT event seems to be associated with a large discontinuity in the solar wind, intensification of the interplanetary magnetic field (IMF), sign change in all 3 IMF components, and a large drop in solar wind density. These characteristics could define one kind of event that leads to strong pitch angle diffusion. During these events, an initial loss of electrons at all pitch angles is observed, with the pitch angle distribution shifting from a distribution peaked around 90° to a more isotropic distribution as electron flux increases. A concurrent increase in the parallel flux is also observed.

6. Summary

[43] During 27 February 2012, a moderate geomagnetic disturbance began to influence the outer radiation belt. At about 13 UT, the outer radiation belt fluxes from 100 keV to 1 MeV began to decline, with the earliest onset occurring at higher L shells. Following EEP events at 18 and 20 UT, the radiation belt trapped fluxes <600 keV were dramatically enhanced, in contrast to the >800 keV fluxes which continued to decline. Several strong EEP events were observed, i.e., at 02, ~15, 18, and 20 UT, but they seem to be superimposed on, rather than the cause of, the decline in the outer radiation belt fluxes.

[44] The findings of this study can be summarized as follows:

[45] 1. In the 02 UT event, loss of trapped electrons was observed over a wide range of energies, i.e., 30–600 keV, >800 keV, and >2 MeV, particularly over the $L = 5$–7 range. Precipitation was observed from $L = 4$–6, with a preevent buildup of parallel-orientated electrons, suddenly lost during the event. The event does not appear to be a large, classical substorm because of the narrow range of L shells involved in the EEP. However, GOES magnetometer data at the time indicate a large stretching of the magnetic field, with a subsequent dipolarization, confirming the occurrence of a substorm.

[46] 2. Large differences were found between the precipitation flux at ~02 UT observed by instruments on the ground and those observed by POES, suggesting a weak diffusion process only partially filling the BLC. No long-lasting effects on the trapped fluxes were observed.

[47] 3. The 18 and 20 UT events are superimposed on a declining outer radiation belt, which started around 13 UT. The events themselves show increases in both trapped and precipitating fluxes over a wide range of energies (i.e., 30 keV to 2 MeV) and a wide range of L shells (i.e., $L = 3.5$–10). The variations in anisotropy and PSD suggest a transport mechanism acting on the radiation belt electrons.

[48] 4. The ground-based observations indicate EEP flux levels that are similar to those observed by POES, which are consistent with a strong diffusion mechanism filling the BLC. Following these events, the radiation belt trapped fluxes <600 keV remain enhanced, possibly because the EEP has stopped. However, the relativistic fluxes remain low.

[49] 5. The EEP events are clearly part of the process that triggers the recovery of the outer radiation belt to a flux dropout, and the GOES PSD analysis suggests that this is due to adiabatic transport of electrons.

[50] Overall, this study period shows similarities with the picture of electron precipitation and loss during a flux dropout event as described by *Hendry et al*. [2012]. The reduction in the background radiation belt fluxes that began at 13 UT on 27 February 2012 does not appear to be related to any individual EEP events. However, several EEP events occurred between 15 and 20 UT, with the final one causing electron energies of <600 keV to remain elevated and produce the well-known picture of a flux dropout event at high electron energies (~1 MeV) with enhanced lower-energy fluxes. Enhanced VLF chorus waves were observed at Halley, Antarctica, at the time of the 20 UT event, whereas electromagnetic ion cyclotron waves were absent, although it is unclear if the chorus was instrumental in the radiation belt recovery as the waves were only observed for as long as the EEP event itself.

[51] **Acknowledgments.** M.A.C. and N.C.O. would like to acknowledge the important contributions from Nick Alford and Tom Stroud, particularly for their skill and assistance in building and deploying the Autonomous AARDDVARK systems. The authors would like to thank the Space Physics Data Facility (SPDF) for providing the solar and geomagnetic data. The research leading to these results has received funding from the Natural Environmental Research Council under the Antarctic Funding Initiative (AFI/11/22). C.J.R. was supported by the New Zealand Marsden Fund. M. H.D. was supported by STFC grant ST/I000801/1 and D.H. was supported by a STFC PhD Studentship. And J.V.R. was supported by the GOES-R Risk Reduction Program.

[52] Robert Lysak thanks Nikolai G. Lehtinen and an anonymous reviewer for their assistance in evaluating this paper.

References

Baker, D. N. (2002), How to cope with space weather, *Science*, *297*(5586), 1486–1487, doi:10.1126/science.1074956.

Barr, R., D. L. Jones, and C. J. Rodger (2000), ELF and VLF radio waves, *J. Atmos. Sol. Terr. Phys.*, *62*, 1689–1718.

Borovsky, J. E., and M. H. Denton (2010), The magnetic field at geosynchronous orbit during high-speed-stream-driven storms: Connections to the solar wind, the plasma sheet, and the outer electron radiation belt, *J. Geophys. Res.*, *115*, A08217, doi:10.1029/2009JA015116.

Clilverd, M. A., C. J. Rodger, T. Ulich, A. Seppälä, E. Turunen, A. Botman, and N. R. Thomson (2005), Modeling a large solar proton event in the southern polar atmosphere, *J. Geophys. Res.*, *110*, A09307, doi:10.1029/2004JA010922.

Clilverd, M. A., et al. (2008a), Energetic electron precipitation during substorm injection events: High-latitude fluxes and an unexpected midlatitude signature, *J. Geophys. Res.*, *113*, A10311, doi:10.1029/2008JA013220.

Clilverd, M. A., C. J. Rodger, R. J. Gamble, N. P. Meredith, M. Parrot, J.-J. Berthelier, and N. R. Thomson (2008b), Ground based transmitter signals observed from space: Ducted or nonducted?, *J. Geophys. Res.*, *113*, A04211, doi:10.1029/2007JA012602.

Clilverd, M. A., et al. (2009), Remote sensing space weather events: The AARDDVARK network, *Space Weather*, *7*, S04001, doi:10.1029/2008SW000412.

Clilverd, M. A., C. J. Rodger, R. J. Gamble, T. Ulich, T. Raita, A. Seppälä, J. C. Green, N. R. Thomson, J.-A. Sauvaud, and M. Parrot (2010), Ground-based estimates of outer radiation belt energetic electron precipitation fluxes into the atmosphere, *J. Geophys. Res.*, *115*, A12304, doi:10.1029/2010JA015638.

Clilverd, M. A., C. J. Rodger, I. J. Rae, J. B. Brundell, N. R. Thomson, N. Cobbett, P. T. Verronen, and F. W. Menk (2012a), Combined THEMIS and ground-based observations of a pair of substorm-associated electron precipitation events, *J. Geophys. Res.*, *117*, A02313, doi:10.1029/2011JA016933.

Clilverd, M. A., C. J. Rodger, D. Danskin, M. E. Usanova, T. Raita, T. Ulich, and E. L. Spanswick (2012b), Energetic particle injection, acceleration, and loss during the geomagnetic disturbances which upset Galaxy 15, *J. Geophys. Res.*, *117*, A12213, doi:10.1029/2012JA018175.

Denton, M. H., and J. E. Borovsky (2008), Superposed epoch analysis of high-speed-stream effects at geosynchronous orbit: Hot plasma, cold plasma, and the solar wind, *J. Geophys. Res.*, *113*, A07216, doi:10.1029/2007JA012998.

Engebretson, M. J., et al. (2008), Pc1–Pc2 waves and energetic particle precipitation during and after magnetic storms: Superposed epoch analysis and case studies, *J. Geophys. Res.*, *113*, A01211, doi:10.1029/2007JA012362.

Evans, D. S., and M. S. Greer (2004), Polar orbiting environmental satellite space environment monitor-2 instrument descriptions and archive data documentation, NOAA Technical Memorandum version 1.4, Space Environment Laboratory, Boulder, Colo.

Ferguson, J. A., and F. P. Snyder (1990), Computer programs for assessment of long wavelength radio communications, Tech. Doc. 1773, Natl. Ocean Syst. Cent., San Diego, Calif.

Fok, M.-C., R. B. Horne, N. P. Meredith, and S. A. Glauert (2008), Radiation belt environment model: Application to space weather nowcasting, *J. Geophys. Res.*, *113*, A03S08, doi:10.1029/2007JA012558.

Gamble, R. J., C. J. Rodger, M. A. Clilverd, J. A. Sauvaud, N. R. Thomson, S. L. Stewart, R. J. McCormick, M. Parrot, and J.-J. Berthelier (2008), Radiation belt electron precipitation by man-made VLF transmissions, *J. Geophys. Res.*, *113*, A10211, doi:10.1029/2008JA013369.

Green, J. C., and M. G. Kivelson (2004), Relativistic electrons in the outer radiation belt: Differentiating between acceleration mechanisms, *J. Geophys. Res.*, *109*, A03213, doi:10.1029/2003JA010153.

Hanser, F. A. (2011), EPS/HEPAD calibration and data handbook, Tech. Rep. GOESN-ENG-048D, Assurance Technol. Corp., Carlisle, Mass.

Hartley, D. P., M. H. Denton, J. C. Green, T. G. Onsager, J. V. Rodriguez, and H. J. Singer (2013), Case studies of the impact of high-speed solar-wind streams on the electron radiation belt at geosynchronous orbit: Flux, magnetic field and phase space density, *J. Geophys. Res. Space Physics*, doi:10.1002/2013JA018923.

Hendry, A. T., C. J. Rodger, M. A. Clilverd, N. R. Thomson, S. K. Morley, and T. Raita (2012), Rapid radiation belt losses occurring during high speed solar wind stream driven storms: Importance of energetic electron precipitation, in *Dynamics of the Earth's Radiation Belts and Inner Magnetosphere*, Geophys. Monogr. Ser., vol. 199, edited by D. Summers et al., pp. 213–223, AGU, Washington, D. C., doi:10.1029/2012GM001299.

Horne, R. B. (2002), The contribution of wave-particle interactions to electron loss and acceleration in the Earth's radiation belts during geomagnetic storms, in *URSI Review of Radio Science 1999–2002*, edited by W. R. Stone, pp. 801–828, Wiley, New York.

Horne, R. B., et al. (2005), Wave acceleration of electrons in the Van Allen radiation belts, *Nature*, *437*, 227–230.

Lam, M. M., R. B. Horne, N. P. Meredith, S. A. Glauert, T. Moffat-Griffin, and J. C. Green (2010), Origin of energetic electron precipitation >30 keV into the atmosphere, *J. Geophys. Res.*, *115*, A00F08, doi:10.1029/2009JA014619.

Lam, H.-L., D. H. Boteler, B. Burlton, and J. Evans (2012), Anik-E1 and E2 satellite failures of January 1994 revisited, *Space Weather*, *10*, S10003, doi:10.1029/2012SW000811.

Little, C. G., and H. Leinbach (1959), The riometer: A device for the continuous measurements of ionospheric absorption, *Proc. IRE*, *37*, 315–320.

Maalouf, M., M. Durante, and N. Foray (2011), Biological effects of space radiation on human cells: History, advances and outcomes, *J. Radiation Res.*, *52*(2), 126–146, doi:10.1269/jrr.10128.

McRae, W. M., and N. R. Thomson (2000), VLF phase and amplitude: Daytime ionospheric parameters, *J. Atmos. Sol. Terr. Phys.*, *62*(7), 609–618.

Millan, R. M., K. Yando, and J. C. Green (2008), NOAA POES observations of relativistic electron precipitation during a radiation belt depletion event, *Eos Trans. AGU*, *89*(53), Fall Meet. Suppl., U13A–0043.

Miyoshi, Y., and R. Kataoka (2008), Flux enhancement of the outer radiation belt electrons after the arrival of stream interaction regions, *J. Geophys. Res.*, *113*, A03S09, doi:10.1029/2007JA012506.

Morley, S. K., R. H. W. Friedel, T. E. Cayton, and E. Noveroske (2010), A rapid, global and prolonged electron radiation belt dropout observed with the Global Positioning System constellation, *Geophys. Res. Lett.*, *37*, L06102, doi:10.1029/2010GL042772.

Onsager, T. G., R. Grubb, J. Kunches, L. Matheson, D. Speich, R. Zwickl, and H. Sauer (1996), Operational uses of the GOES energetic particle detectors, in GOES-8 and Beyond: 7–9 August 1996, Denver, Colorado, edited by E. R. Washwell, Proc. SPIE Int. Soc. Opt. Eng., 2812, 281.

Paulikas, G. A., and J. B. Blake (1979), Effects of the solar wind on magnetospheric dynamics: Energetic electrons at the synchronous orbit, in *Quantitative Modeling of Magnetospheric Processes*, Geophys. Monogr. Ser., vol. 21, edited by W. P. Olsen, pp. 180–202, AGU, Washington, D. C., doi:10.1029/GM021p0180.

Randall, C. E., et al. (2005), Stratospheric effects of energetic particle precipitation in 2003–2004, *Geophys. Res. Lett.*, *32*, L05802, doi:10.1029/2004GL022003.

Rodger, C. J., O. A. Molchanov, and N. R. Thomson (1998), Relaxation of transient ionization in the lower ionosphere, *J. Geophys. Res.*, *103*(4), 6969–6975.

Rodger, C. J., M. A. Clilverd, N. R. Thomson, R. J. Gamble, A. Seppälä, E. Turunen, N. P. Meredith, M. Parrot, J. A. Sauvaud, and J.-J. Berthelier (2007), Radiation belt electron precipitation into the atmosphere: Recovery from a geomagnetic storm, *J. Geophys. Res.*, *112*, A11307, doi:10.1029/2007JA012383.

Rodger, C. J., M. A. Clilverd, J. Green, and M.-M. Lam (2010a), Use of POES SEM-2 observations to examine radiation belt dynamics and energetic electron precipitation in to the atmosphere, *J. Geophys. Res.*, *115*, A04202, doi:10.1029/2008JA014023.

Rodger, C. J., B. R. Carson, S. A. Cummer, R. J. Gamble, M. A. Clilverd, J.-A. Sauvaud, M. Parrot, J. C. Green, and J.-J. Berthelier (2010b), Contrasting the efficiency of radiation belt losses caused by ducted and non-ducted whistler mode waves from ground-based transmitters, *J. Geophys. Res.*, *115*, A12208, doi:10.1029/2010JA015880.

Rodger, C. J., M. A. Clilverd, A. J. Kavanagh, C. E. J. Watt, P. T. Verronen, and T. Raita (2012), Contrasting the responses of three different ground-based instruments to energetic electron precipitation, *Radio Sci.*, *47*, RS2021, doi:10.1029/2011RS004971.

Sandanger, M., F. Søraas, K. Aarsnes, K. Oksavik, and D. S. Evans (2007), Loss of relativistic electrons: Evidence for pitch angle scattering by electromagnetic ion cyclotron waves excited by unstable ring current protons, *J. Geophys. Res.*, *112*, A12213, doi:10.1029/2006JA012138.

Selesnick, R. S., and J. B. Blake (2000), On the source location of radiation belt relativistic electrons, *J. Geophys. Res.*, *105*(A2), 2607–2624, doi:10.1029/1999JA900445.

Smith, A. J. (1995), VELOX: A new VLF/ELF receiver in Antarctica for the Global Geospace Science mission, *J. Atmos. Terr. Phys.*, *57*, 507–524.

Thomson, N. R., M. A. Clilverd, and C. J. Rodger (2011a), Daytime midlatitude D region parameters at solar minimum from short-path VLF phase and amplitude, *J. Geophys. Res.*, *116*, A03310, doi:10.1029/2010JA016248.

Thomson, N. R., C. J. Rodger, M. A. Clilverd (2011b), Daytime D region parameters from long-path VLF phase and amplitude, *J. Geophys. Res.*, *116*, A11305, doi:10.1029/2011JA016910.

Thorne, R. M. (2010), Radiation belt dynamics: The importance of wave-particle interactions, *Geophys. Res. Lett.*, *37*, L22107, doi:10.1029/2010GL044990.

Tsyganenko, N. A., and D. P. Stern (1996), Modeling the global magnetic field of the large-scale Birkeland current systems, *J. Geophys. Res.*, *101*, 27,187–27,198.

Turner, D. L., et al. (2012), Explaining sudden losses of outer radiation belt electrons during geomagnetic storms, *Nat. Phys.*, *8*, 208–121, doi:10.1038/nphys2185.

Westerlund, S., F. H. Reder, and C. Abom (1969), Effects of polar cap absorption events on VLF transmissions, *Planet. Space Sci.*, *17*, 1329–1374.

Yando, K., R. M. Millan, J. C. Green, and D. S. Evans (2011), A Monte Carlo simulation of the NOAA POES Medium Energy Proton and Electron Detector instrument, *J. Geophys. Res.*, *116*, A10231, doi:10.1029/2011JA016671.